

ARTICLE

Open Access

Simple and robust 3D MINFLUX excitation with a variable phase plate

Takahiro Deguchi¹ and Jonas Ries^{1,2,3,4}✉

Abstract

MINFLUX has achieved extraordinary resolution in superresolution imaging and single fluorophore tracking. It is based on localizing single fluorophores by rapid probing with a patterned beam that features a local intensity minimum. Current implementations, however, are complex and expensive and are limited in speed and robustness. Here, we show that a combination of an electro-optical modulator with a segmented birefringent element such as a spatial light modulator produces a variable phase plate for which the phase can be scanned on the MHz timescale. Bisected or top-hat phase patterns generate high-contrast compact excitation point-spread functions for MINFLUX localization in the x, y, and z-direction, respectively, which can be scanned across a fluorophore within a microsecond, switched within 60 microseconds and alternated among different excitation wavelengths. We discuss how to compensate for non-optimal performance of the components and present a robust 3D and multi-color MINFLUX excitation module, which we envision as an integral component of a high-performance and cost-effective open-source MINFLUX.

Introduction

MINFLUX¹ is a super-resolution microscopy technique in which a patterned beam featuring a local intensity minimum, typically a donut beam, probes the signal around a single fluorophore. From the intensities measured at different locations, the position of the fluorophore can be estimated. Recentering of the scan pattern on the estimated position and decreasing its size in an iterative way proves to be more effective in enhancing localization precision compared to increasing photon numbers. This means that for a given number of photons emitted by the fluorophore MINFLUX outperforms camera-based Single-Molecule Localization Microscopy (SMLM)² in terms of localization precision. MINFLUX has been used for high-resolution imaging in fixed^{3,4} and live² cells and for tracking single fluorophores with unprecedented spatio-temporal resolution^{5–7}.

For optimal performance, a MINFLUX microscope requires fast and repeated scanning of the pattern to average over potential intensity fluctuations of the

fluorophore. In most custom^{2,5} and commercial⁸ microscopes, a donut-shaped beam, created by a vortex phase pattern, is scanned laterally using electro-optical deflectors. For 3D MINFLUX, typically a top-hat phase pattern that results in a ‘3D donut’ is employed and axial scanning is performed with an electro-optically actuated varifocal lens² or a deformable mirror⁸. All these fast 3D scanning solutions require expensive components. Standard confocal microscopes with galvo scanners can be upgraded to the MINFLUX mode by insertion of a vortex phase plate⁹, but these implementations might not easily reach the resolution and speed of dedicated MINFLUX instruments. Pulsed interleaved MINFLUX¹⁰ replaces the lateral scanning with four optical fibers of different lengths at the cost of flexible scan patterns, which in combination with a pulsed laser allows switching between donut positions within 12.5 ns and provides information on fluorescence lifetime. Recently, interference of two beams was used to create bilobed excitation patterns that could be rapidly scanned across a single fluorophore by changing the interference phase with an electro-optical modulator (EOM)⁶. Still, generating a pattern for 3D MINFLUX in multiple colors that features rapid scanning with sub-nanometer accuracy and stability is challenging and can be costly.

Correspondence: Jonas Ries (Jonas.ries@univie.ac.at)

¹European Molecular Biology Laboratory, Cell Biology and Biophysics, Heidelberg, Germany

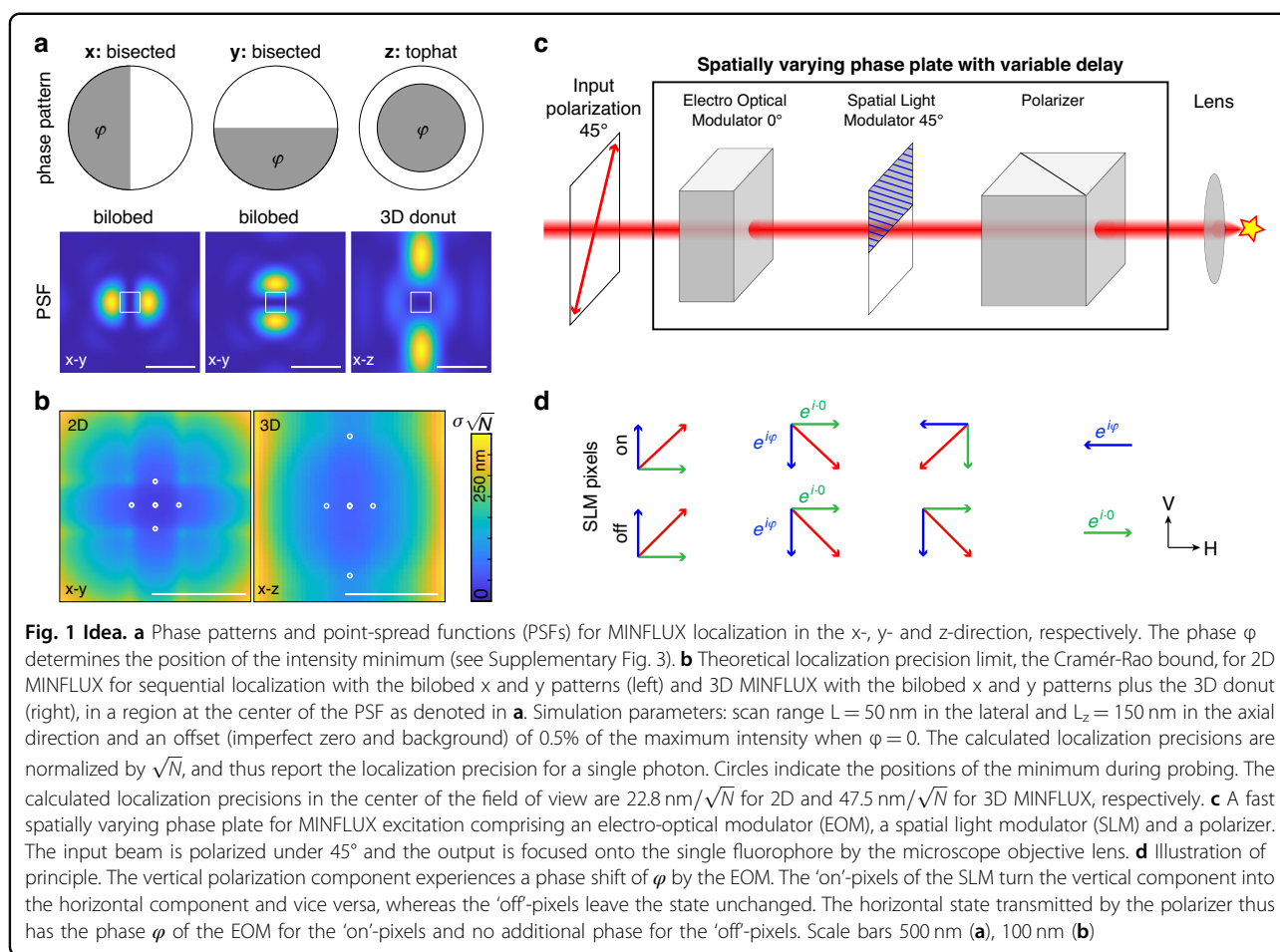
²Max Perutz Labs, Vienna Biocenter Campus (VBC), Vienna, Austria

Full list of author information is available at the end of the article

© The Author(s) 2024



Open Access This article is licensed under a Creative Commons Attribution 4.0 International License, which permits use, sharing, adaptation, distribution and reproduction in any medium or format, as long as you give appropriate credit to the original author(s) and the source, provide a link to the Creative Commons licence, and indicate if changes were made. The images or other third party material in this article are included in the article's Creative Commons licence, unless indicated otherwise in a credit line to the material. If material is not included in the article's Creative Commons licence and your intended use is not permitted by statutory regulation or exceeds the permitted use, you will need to obtain permission directly from the copyright holder. To view a copy of this licence, visit <http://creativecommons.org/licenses/by/4.0/>.



Results

Here, we overcome this challenge by developing a MINFLUX excitation module based on a novel variable phase plate, which enables 3D multi-color MINFLUX with high spatio-temporal resolution using a simple, robust, and economic setup.

This module generates high-contrast MINFLUX PSFs and scans them rapidly across a fluorophore. However, it is only one component of a fully functional MINFLUX microscope, which additionally requires real-time feedback of the position estimate on the scan pattern and a very stable microscope body combined with active sample stabilization with sub-nanometer accuracy. The construction of such a complete MINFLUX microscope is complex and out of scope for this article. Instead, we experimentally demonstrate the generation and fast scanning of optimized MINFLUX PSFs with a low-NA setup, show with simulations that this setup can be directly transferred to high-NA microscopes without loss in performance, and discuss how to overcome experimental imperfections that otherwise might limit the quality of the PSFs.

Simple phase patterns for one-dimensional MINFLUX localization

As shown by Wirth et al.⁶, the use of distinctive PSFs for each dimension can outperform the donut-shaped beam profiles generated by a vortex phase pattern. In this work, we use 3 simple binary phase patterns that generate compact MINFLUX beams for x-, y-, and z-localization, respectively (Fig. 1a). For 2D MINFLUX these bilobed PSFs¹¹ achieve a similar localization precision compared to donut or interference phase patterns for a given number of detected photons (Fig. 1b, Supplementary Fig. 1). Due to their small size, they allow for a higher density of fluorophores than the donut beam. Because of their compactness they require lower laser powers (Supplementary Fig. 2A, B), which reduces a background due to an imperfect PSF minimum, auto-fluorescence and out-of-focus fluorescence. This leads to a lower intensity at the minimum and consequently to an improved localization precision (Supplementary Fig. 2C, D). For 3D MINFLUX the combination of specific patterns achieves a substantially better localization precision compared to using the '3D

donut' alone (Supplementary Fig. 1). Importantly, the bi-lobed PSFs have a much larger field of view compared to donut PSFs (Supplementary Fig. 2D), i.e., the localization precision decreases much slower with the distance of the fluorophore from the center of the scan pattern. Thus, they require a lower number of iterations with decreasing L , which leads to improved speed and fewer lost photons during the initial coarse localization process. The position estimation can be performed separately for each dimension with a simple analytical 1D estimator⁶, which reduces the complexity and increases the speed when implemented on an FPGA for real-time feedback.

Phase differences of π give rise to symmetric patterns with the minimum on the optical axis (x, y pattern) or in the focus of the objective lens (z pattern), because here the π phase shift leads to destructive interference. Phase differences different from π displace the position of the minimum because the rays must acquire an additional path difference to reach a phase difference of π (Supplementary Fig. 3). Simulations show that for the bilobed PSFs a true zero at the minimum is preserved even for high-NA systems and large scanning, whereas for the 3D donut the contrast stays high over a z range of a few hundred nm (Supplementary Fig. 4).

The phase patterns can be created with a spatial light modulator (SLM), which, in principle, can scan the position of the intensity minimum by changing the phase. However, SLMs that produce continuous phase delays are too slow (<1 kHz) for the rapid scanning required for MINFLUX, thus a fast scanner like an electro optical deflector would still be required.

A fast variable phase plate based on polarization optics

Here we overcome this limitation by combining an EOM, an SLM and a polarizer to generate binary phase patterns with variable phase delay, where the phase delay can be changed on the sub-microsecond time scale by the EOM phase (Fig. 1c, d). The input laser beam is polarized under 45° and enters the EOM for which the polarization axis is oriented vertically under 0° . The EOM can thus cause a phase delay between the vertical and the horizontal polarization component of the beam. The binary SLM is oriented in a way that the 'off'-pixels (dark pixels of the imposed phase pattern) do not change the polarization state, whereas the 'on'-pixels (bright pixels) act as a half-wave plate (HWP) oriented at 45° , which rotate the vertical polarization component into the horizontal polarization. This component carries the extra phase imposed by the EOM. A polarizer (e.g., a polarizing beam splitter) transmits only the horizontal component, which has no extra phase for 'off'-pixels of

the SLM and the phase imposed by the EOM for 'on'-pixels.

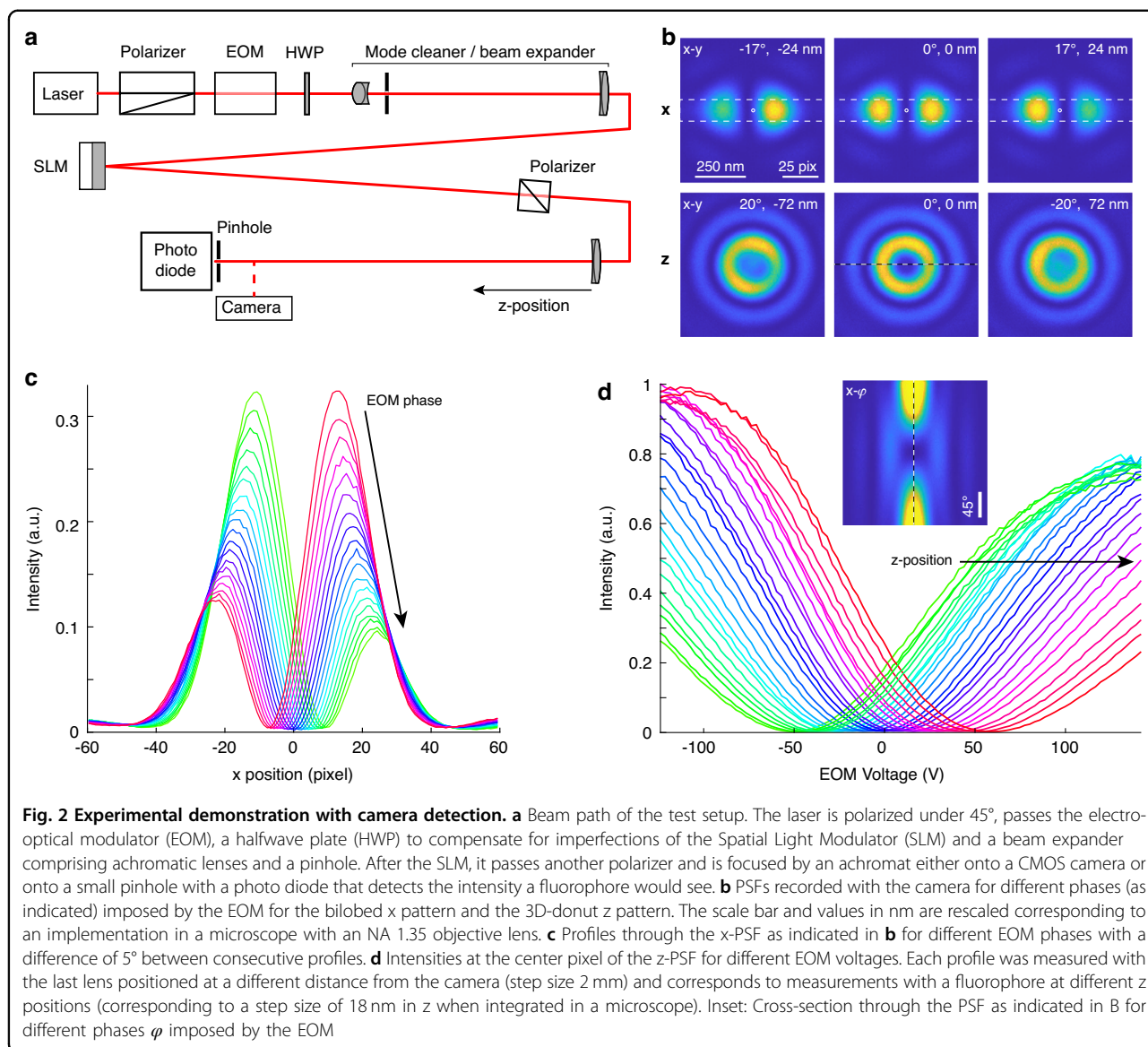
Using Jones matrices, we can calculate in the horizontal/vertical coordinate system that an input beam of $E_{\text{in}} = \frac{E_0}{\sqrt{2}} \begin{pmatrix} 1 \\ 1 \end{pmatrix}$ acquires a phase of $E_{\text{EOM}} = \frac{E_0}{\sqrt{2}} \begin{pmatrix} 1 \\ e^{i\varphi} \end{pmatrix}$ after the EOM. The 'on'-pixels of the SLM result in $E_{\text{SLM}} = \frac{E_0}{\sqrt{2}} \begin{pmatrix} e^{i\varphi} \\ 1 \end{pmatrix}$, whereas the 'off'-pixels do not change the polarization state. After the polarizer the state is $E_{\text{off}} = \frac{E_0}{\sqrt{2}} \begin{pmatrix} 1 \\ 0 \end{pmatrix}$ for the 'off'-pixels and $E_{\text{on}} = \frac{E_0}{\sqrt{2}} e^{i\varphi} \begin{pmatrix} 1 \\ 0 \end{pmatrix}$ for the 'on'-pixels. When both components interfere in the vicinity of the focus of the objective lens, the intensity is $I = |E_{\text{off}} + E_{\text{on}}|^2 = E_0^2(1 + \cos(\varphi - \xi))$. ξ describes an additional phase difference depending on distance to the focal point.

Experimental demonstration

To experimentally validate our idea without the need of implementing a complete MINFLUX microscope, we designed a beam path in which we replaced the objective lens by an $f=400$ mm achromat and the single fluorophore by a small pinhole and photo detector that reports the intensity at the putative single-fluorophore position (Fig. 2a). Additionally, we imaged the MINFLUX PSFs with a CMOS camera.

The bisected phase patterns produced the expected bilobed PSFs (Fig. 2b, c) with high contrast. By changing the EOM phase, we could scan these patterns laterally with only a minimal loss in contrast (Fig. 2c). The top-hat phase pattern produced a high-contrast circular illumination pattern in the focus, and a change in the EOM phase led to an increased signal in the center (Fig. 2b). Indeed, when placing the achromat at different distances from the pinhole, which effectively changes the pinhole's z -position, the signal was minimal at different EOM phases, demonstrating that the minimum of the '3D donut' can be scanned in z without degradation (Fig. 2d).

To mimic the excitation signal seen by a single fluorophore, we placed a tiny pinhole (0.03 Airy Units) in the focus of the achromat, which transmits the intensity in the central part of the PSF (Fig. 3a). We measured the intensity with an amplified photo diode while changing the EOM phase. Specifically, we alternated the x, y and z phase patterns on the SLM and produced a linear EOM phase ramp for each pattern. The intensity trace showed pronounced minima for each phase pattern with an excellent contrast (minimum relative to the intensity detected from an Airy PSF created by a flat phase pattern) of 0.2%, 0.3%, and 0.2% for the x, y , and z phase patterns, respectively (Fig. 3b).



Next, we tested the speed of our MINFLUX excitation module by repeatedly applying three different EOM phases, which positions the x-PSF at 3 positions around the pinhole that mimics the fluorophore. With excitation times as low as 1 μ s per position we could reliably detect three different intensity values with high contrast (Fig. 3c, Supplementary Fig. 5). This leads to \sim 60 scanning cycles within the 180 μ s localization time that we use for each coordinate. Note that the 3D localization time is limited by the switching time of the SLM (60 μ s).

Multi-color MINFLUX excitation can be realized with the same setup without modifications by using as an input co-linear laser beams. In case of small distances between the fluorophores and low spectral dependence of the phase delay φ , both lasers can be used simultaneously. Otherwise, both lasers can be alternated (Fig. 3e). As

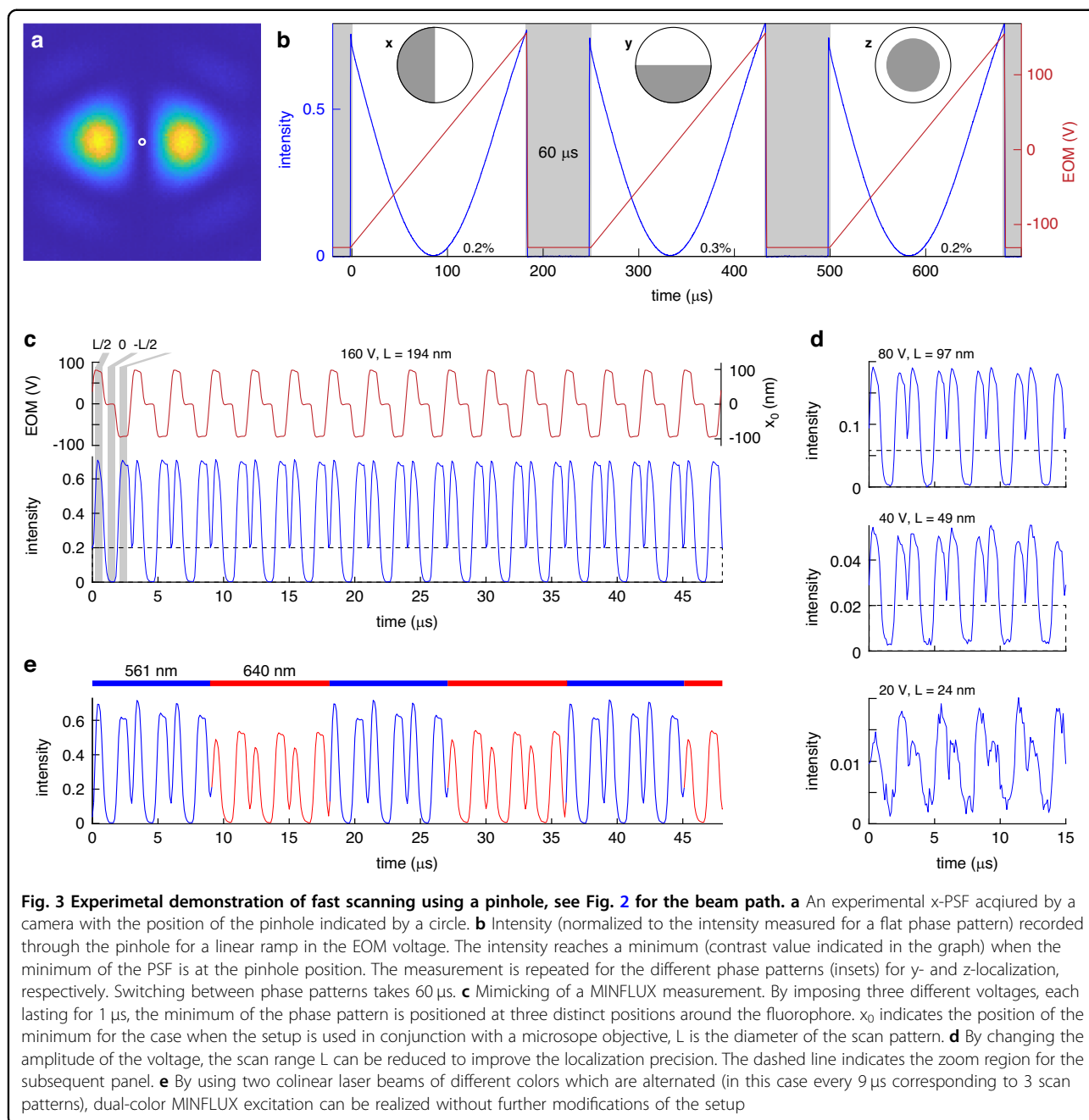
switching between the lasers takes less than one microsecond, the colors can be alternated many times within one MINFLUX localization time, leading to quasi-simultaneous localization of two or more fluorophores.

Non-ideal performance of optical components

The simple schematic in Fig. 1 is based on ideal performance of the optical elements. Here we discuss the impact of non-ideal performance and experimental challenges and present mitigation strategies.

SLM

The binary Ferroelectric Liquid Crystal on Silicon (FLCoS) SLM used here has the birefringent axis of the ‘on’-pixels oriented under 33.5° compared to the ‘off’-pixels, instead of the ideal 45°. Additionally, the phase



delay might deviate slightly from π . By calculations (Methods, Data and code availability) and experimentally we found that the addition of a HWP in the beam path before the SLM can perfectly compensate for both imperfections (Fig. 2a, Supplementary Fig. 6). In addition, the SLM requires ‘balancing’, meaning that for every pixel the time in the ‘on’-state needs to be equal to the time in the ‘off’-state within a 50 ms window. By adjusting the static offset of the EOM phase, the inverse phase map can be matched to the original one, avoiding a reduced duty cycle due to balancing. Finally, the SLM has a finite

switching time between different patterns of $\sim 60 \mu\text{s}$ (40 μs with temperature control), leading to a tradeoff between switching speed and duty cycle. If higher speeds are needed, a separate excitation unit can be used for each of the directions.

EOM

The EOM phase delay is wavelength dependent, leading to larger displacements of the minima for shorter wavelengths for a given EOM voltage. To compensate this, the static offset of the EOM phase, as well

as the amplitude of the phase scan can be set separately for different excitation colors.

Any instability of the EOM phase directly causes a localization bias (1.4 nm/deg in x and y , 3.6 nm/deg in z , see Supplementary Fig. 7). We monitored the EOM phase drift using a second crossed polarizer and photo diode by scanning the EOM phase around the intensity minimum and found phase drifts below 0.2° (corresponding to 0.3 nm for an NA 1.35 system) within 10 s and below 1.1° (1.6 nm) over hours (Supplementary Fig. 7). This setup could be used in the future for passive phase monitoring or active phase stabilization. Alternatively, our low-NA setup using a pinhole and photo diode (Fig. 2a) can be added also to a full MINFLUX microscope. Then, continuous MINFLUX localization of the pinhole creates a spatial reference to passively correct or actively adjust the zero voltage of the EOM, and this for every color separately.

Silver mirrors

Most mirrors, including silver mirrors, lead to a phase delay between the s and p polarization components, which can spoil carefully engineered polarization states. By aligning the EOM in along the s/p coordinate system and placing the polarizer directly after the SLM, any phase imposed by the mirrors can be compensated by adjusting the static offset of the EOM phase.

Aberrated wave fronts

Laser sources, especially free space diode lasers, can have an imperfect beam profile. Additionally, optical components (wave plates, EOM, mirrors) can further deteriorate the wave front, leading to aberrated PSFs and a reduced contrast of the intensity minimum. Here, whenever possible, we place optical components (EOM, waveplate) before the mode cleaner, which then produces a close to ideal wavefront. To reduce astigmatism and coma introduced by a slightly curved SLM, we choose a small beam size on the SLM. In the future, we will insert a second SLM before the microscope to compensate for aberrations from the objective lens or sample.

Scan range

As MINFLUX is based on a confocal principle, and because EODs and varifocal lenses currently do not allow for de-scanning due to polarization dependency and auto-fluorescence, the scan range in all MINFLUX implementations is limited by the confocal pinhole and a secondary slow, but large range scanner (galvo^{6,8} or piezo tip-tilt mirror^{1,2}) is required for imaging with a field of view that exceeds a few hundred nanometers and for tracking with a track length of that scale. This is true also for our implementation. Here, the useable scan range of the PSF without pinhole is ~ 400 nm in the lateral and ~ 1000 nm in the axial direction before the asymmetry of

the PSF leads to a low steepness of the PSF around the minimum (Supplementary Fig. 4A, B). In the axial direction, the contrast decreases for a scan range above ~ 800 nm (Supplementary Fig. 4C). The change of the PSF shape during scanning can be easily taken into account during the position estimation as in Wirth et al.⁶, where the interferometric PSFs show a similar shape change.

Polarization of MINFLUX PSFs

For high-NA microscopes, the x and y phase patterns require the polarization to be parallel to the phase boundary, which can be fulfilled only for one of the directions. Otherwise, the axial component of the electric field leads to incomplete destructive interference and an increased intensity in the minimum of the PSF (Supplementary Fig. 8). One solution is to reflect the beam for a second time on the SLM and rotate the polarization state only for the x pattern (Supplementary Fig. 8). The non-ideal direction of the birefringent axis can only rotate the polarization by 67° leading to a calculated deviation of at least 11.5° from the optimal polarization for both the x and y patterns. This results in a contrast of not better than 0.6% (Supplementary Fig. 8) for an NA 1.35 objective, which however is still acceptable (see Supplementary Fig. 2C). A more accurate alternative is to add a second EOM to the output beam path to generate an optimal polarization state for each phase pattern. This would also allow turning the direction of the phase pattern on the SLM and match it to the sample (e.g., direction of motion of a motor protein) for ultra-fast 1D MINFLUX⁶.

Discussion

We developed an excitation module for 3D and multi-color MINFLUX that combines fast and precise positioning of the intensity minimum with a robust and affordable setup. Although we tested the module only in a low-NA setup, the integration into a full MINFLUX microscope is straightforward as long as the other challenges (fast FPGA-based position feedback, ultra-stable microscope) are met. We performed extensive vectorial wave simulations for a high-NA objective (Supplementary Fig. 4) that show that the high contrast of the PSFs will be retained.

MINFLUX relies on the brightness of the fluorophore to be constant during probing of intensities around the fluorophore and any intensity fluctuations on time scales longer than a fraction of the probing time at a single location can lead to a position bias. Most fluorophores show transient dark states on the microsecond to millisecond time scale^{12,13} due to intersystem crossing, cis-trans isomerization, and transient interactions with small molecules such as thiols or protonation-deprotonation¹⁴. The high probing speed in our approach (1 microsecond per position) allows for many

probing cycles within one 1D localization, which effectively averages out a bias caused by this flickering. In addition, it allows for more complex scanning patterns with a larger number of positions. It remains to be explored if this can improve the background estimation and localization precision.

Whereas 1D localization is sufficient for a few applications such as tracking of linear motor proteins⁶, in general 2D or 3D localization is required. The time resolution for this is limited in our approach by the SLM switching time (60 μ s), leading to a deadtime of \sim 126 μ s for one 2D and \sim 189 μ s for one 3D localization (three probing cycles). In comparison, the deadtime for one 3D localization with a commercial MINFLUX instrument using a deformable mirror was 318 μ s⁸, and with a custom MINFLUX using an electro-optical varifocal lens it was 498 μ s².

The ability to switch quickly between different phase patterns allowed us to use an optimized PSF for each dimension. The bilobed PSFs that we use for lateral localization result in a high precision for a given number of detected photons (Supplementary Fig. 1). They have a smaller footprint compared to donut¹ or interferometric PSFs⁶, and especially compared to the 3D donut used for 3D MINFLUX², and are thus more robust for higher densities of fluorophores. More importantly, they require lower laser powers, leading to reduced background and ultimately improved localization precisions (Supplementary Figs. 1 and 2).

Currently, multi-color MINFLUX is performed sequentially with different fluorophores, or using a single excitation laser in combination with fluorophores of slightly different emission wavelengths². This however precludes using MINFLUX for co-tracking of two colors simultaneously. In principle, multi-color MINFLUX could be implemented by duplicating the excitation beam path for each color. With our implementation, however, this is not necessary, as the same excitation module can be used for simultaneous or quasi-simultaneous MINFLUX localization of two fluorophores or more.

As all beams are colinear and are not split up to generate different patterns, colors, or interference phases, they cannot misalign with respect to each other. Thus, our setup is intrinsically robust and stable, which is essential to reach sub-nanometer accuracies in MINFLUX and to use it for routine biological applications. Stability is further supported by the simplicity of the setup with few components and short beam paths.

Our MINFLUX excitation module is very cost-effective with the components in Fig. 2a excluding lasers costing approx. 10 k\$. Components and electronics employed for pattern generation and 3D scanning in commercial⁸ and custom² instruments would cost around one order of

magnitude more, necessitating two EODs (e.g., M-311-A, Coonoptics, 2 \times 20 k\$, electronics 8 k\$), one deformable mirror (Multi-C-1.5, Boston Micromachines, 30 k\$) or electro-optical varifocal lens (KLMS2D0700, NTT AT, 75 k\$, electronics 25 k\$) and a continuous spatial light modulator (7 k\$).

We envision our excitation module to be a key element for the future development of an affordable open-source MINFLUX instrument with highest performance.

Methods

Calculation of polarization states and point spread functions

Calculation of polarization states

The polarization state of the beam was calculated in Mathematica (Wolfram) using Jones matrices (Data and code availability). Here, a linearly polarized beam is described by

$$E_{\text{in}} = E_0 \begin{pmatrix} 1 \\ 0 \end{pmatrix}$$

in the horizontal/vertical coordinate system, and a beam with 45° linear polarization by

$$E_{45^\circ} = \frac{E_0}{\sqrt{2}} \begin{pmatrix} 1 \\ 1 \end{pmatrix}$$

A waveplate (e.g., halfwave plate or SLM) with a phase delay of φ and an angle of α with respect to the horizontal axis is described by

$$W(\varphi, \alpha) = \begin{pmatrix} \cos^2\alpha + e^{i\varphi}\sin^2\alpha & (1 - e^{i\varphi})\cos\alpha\sin\alpha \\ (1 - e^{i\varphi})\cos\alpha\sin\alpha & \sin^2\alpha + e^{i\varphi}\cos^2\alpha \end{pmatrix}$$

Note that global phase factors are omitted as they do not affect the intensity distribution. The EOM with a phase delay of φ is described by

$$W_{\text{EOM}}(\varphi) = W(\varphi, 0) = \begin{pmatrix} 1 & 0 \\ 0 & e^{i\varphi} \end{pmatrix}$$

A polarizer transmitting horizontal polarization is described by

$$P = \begin{pmatrix} 1 & 0 \\ 0 & 0 \end{pmatrix}$$

The simple setup (Fig. 1) can then be modeled for on-pixels as:

$$E_{\text{out}} = P \cdot W_{\text{SLM}}\left(\pi, \frac{\pi}{4}\right) \cdot W_{\text{EOM}}(\varphi) \cdot E_{45^\circ}$$

A realistic setup with experimental imperfections is modeled as:

$$E_{\text{out}} = P \cdot W_{\text{SLM}}\left(\pi + d\phi_{\text{SLM}}, \frac{\pi}{4} + d\alpha_{\text{SLM}}\right) \cdot W_{\text{HWP}}(\pi, \alpha) \cdot W_{\text{EOM}}(\varphi) \cdot E_{45^\circ}$$

Here, W_{HWP} describes the additional HWP added to the beam path to compensate for imperfections of the SLM (see section Non-ideal performance of optical components). To determine the optimal orientation of this HWP (Supplementary Fig. 6) we summed up the field for on- and off-pixels to calculate the intensity after destructive interference. For a given combination of $d\phi_{\text{SLM}}$ and $d\alpha_{\text{SLM}}$ we determined numerically the HWP angle α and EOM phase φ that minimized this intensity. We found that this intensity can always be made zero within the numerical precision, showing that a complete compensation of imperfect phase delay or polarization axis direction of the SLM is possible with this HWP (Supplementary Fig. 6, Data and code availability), in line with our experimental finding.

Calculation of MINFLUX point-spread functions

For the numerical calculations of the electromagnetic field near the focus of an objective lens, we used MATLAB (R2022a, MathWorks) and a software package provided by Leutenegger et al.¹⁵. It calculates the electromagnetic field using fast Fourier transforms by taking the vectorial Debye diffraction integral. For the different beam shapes, the phase patterns of the input beam at the back focal plane were modified. We used the following parameters: 100× objective lens, aperture diameter 6.5 mm, numerical aperture 1.35; refractive index 1.406 for the immersion and mounting media; wavelength 635 nm; beam diameter 7.0 mm; flat illumination intensity profile; circular polarization for 3D donut and linear polarization for the rest; and voxel size 2 nm, unless otherwise specified. For the calculation of the interferometric PSF used in Wirth et al.⁶, we used two beams with a Gaussian intensity profile, a beam diameter of 2.3 mm, the beam offset from the center of 2.3 mm, and a relative phase delay of π between the two beams¹⁶.

The background offset is due to an imperfect PSF with a minimum larger than zero and autofluorescence generated by the sample (including out-of-focus fluorophores) and by the optics of the microscope, all of which scale with the total laser intensity. This is why we normalized all PSFs by the total integrated light. To have more interpretable values, we again normalize those so that a Gaussian beam has a maximum intensity of 1. This makes the different PSFs easily comparable in terms of contrast and background offset caused by the total intensity.

Calculation of Cramer-Rao-Bounds (CRBs)

For calculating the theoretically best possible localization precision for specific PSFs, scanning schemes, detected photons and signal to background ratios we followed Masullo et al.¹⁷ (Supplementary Fig. 1, Data and code availability). During MINFLUX localization, the fluorophore at position \mathbf{r}_E is probed with different PSFs $I_i(\mathbf{r}_E)$ to result in K emitter intensities $\mathbf{n} = [n_1, n_2, \dots, n_i, \dots, n_K]$. This includes the case when the PSF is positioned to coordinates \mathbf{r}_i , then $I_i(\mathbf{r}_E) = I(\mathbf{r}_E - \mathbf{r}_i)$, but also the case where the $I_i(\mathbf{r}_E)$ are calculated explicitly. With

$$p_i(\mathbf{r}_E) = \frac{I_i(\mathbf{r}_E)}{\sum_j I_j(\mathbf{r}_E)}$$

the log-likelihood (after dropping of constant terms) can be written as

$$l(\mathbf{r}_E | \mathbf{n}) = \sum_{i=1}^K n_i \ln p_i(\mathbf{r}_E | \mathbf{n})$$

The Fisher information matrix can then be written as:

$$\mathcal{J}(\mathbf{r}_E) = N \sum_{i=1}^K \frac{1}{p_i} \begin{pmatrix} \left(\frac{\partial p_i}{\partial x}\right)^2 & \frac{\partial p_i}{\partial x} \frac{\partial p_i}{\partial y} & \frac{\partial p_i}{\partial x} \frac{\partial p_i}{\partial z} \\ \frac{\partial p_i}{\partial y} \frac{\partial p_i}{\partial x} & \left(\frac{\partial p_i}{\partial y}\right)^2 & \frac{\partial p_i}{\partial y} \frac{\partial p_i}{\partial z} \\ \frac{\partial p_i}{\partial z} \frac{\partial p_i}{\partial x} & \frac{\partial p_i}{\partial z} \frac{\partial p_i}{\partial y} & \left(\frac{\partial p_i}{\partial z}\right)^2 \end{pmatrix}$$

The CRB is then

$$\Sigma_{\text{cov}}(\mathbf{r}_E) \geq \Sigma_{\text{CRB}}(\mathbf{r}_E) = \mathcal{J}(\mathbf{r}_E)^{-1}$$

To account for imperfect contrast and a fluorescent background, we modeled the background explicitly by adding an offset to the PSF. To make the background comparable for different PSFs, we calculated the maximum value $I_A(0)$ of an Airy PSF with a flat phase pattern and equal summed intensity and added the offset $b \cdot I_A(0)$ to the PSF. We chose this approach over using the signal-to-background (SBR) ratio¹⁷, because the latter varies strongly with the PSF and scan pattern. The reported maximum localization precisions are normalized to the input photon counts N as $\sigma_{N=1} = \sigma\sqrt{N}$ and averaged over the dimensions, with $\sigma = \sqrt{(CRB_x + CRB_y)/2}$ for 2D and $\sigma = \sqrt{(CRB_x + CRB_y + CRB_z)/3}$ for 3D. They thus report the localization precision of a single photon.

Optical setup

See Fig. 2a. As a light source we used either an iBeam smart 640 nm laser (Toptica) together with an achromatic halfwave plate (AHWP10M-600, Thorlabs) or a multi-color laser engine (MLE HP, Toptica) together with a

collimator and beam expander (GBE05-A, Thorlabs) to achieve a beam diameter of approx. 1 mm and a polarization direction of around 45°. The beam was adjusted through a Glan-Thompson polarizer aligned at 45° (GTH10M-A, Thorlabs) and an EOM (EO-AM-NR-C4, Thorlabs) that was mounted under 45° with a custom holder so that its birefringent axis was vertical. As the MgO-doped lithium niobate in this EOM displays a slow negation to an applied DC field for wavelengths shorter than approx. 600 nm, we used a different EOM (LM0202 KD*P 3×3, LINOS) for multi-color measurements, also mounted with its birefringent axis aligned along the vertical direction. The beam then passed an achromatic halfwave plate (AHWP10M-600, Thorlabs) that was used to compensate for imperfections of the SLM and a mode cleaner/beam expander consisting of an $f = 40$ mm achromat (Thorlabs), a 20 μm pinhole (Thorlabs) and an $f = 150$ mm achromat (Thorlabs). An iris (SM1D12D, Thorlabs) with a diameter of approx. 2.3 mm resulted in a nearly homogenous beam profile. The beam was then reflected off the SLM (SXGA-R12-STR, Forth Dimension Displays) under an angle of approx. 5°, passed a polarizing beam splitter (PBS251, Thorlabs), and was focused onto a 10 μm pinhole (Thorlabs) with an $f = 400$ mm achromat (Thorlabs). The intensity after the pinhole was monitored with an amplified photo diode (PDA100A2, Thorlabs). Alternatively, the beam was focused onto a CMOS camera (Chameleon CM3-U3-50S5M-CS, Edmund Optics).

Electronic control

The EOM was driven by a voltage amplifier (HVA200, Thorlabs), which was controlled by a function generator (SDG1062X, Siglent). Intensity signals from the photo diode were acquired with an oscilloscope (SDS2104X-Plus, Siglent). The function generator and the oscilloscope were triggered by the SLM at the start of an image sequence. Additionally, the SLM produces a trigger signal when a valid pattern is established, which was used to switch off the lasers during the pattern switching via a TTL signal. Camera images were recorded asynchronously. For dual-color measurements, we used a custom TTL signal converter in combination with the function generator to alternate between the 561 nm and 638 nm laser line.

Note that our time resolution for 1D probing of 1 μs is currently limited by the electronics for EOM scanning and the bandwidth of the photo diode and can in principle be one order of magnitude faster. Such high speeds might not be necessary for MINFLUX but could be useful for other applications of the variable phase plate.

Alignment

We used a polarization analyzer (PAX1000VIS/M, Thorlabs) to align the Glan-Thompson polarizer to 45°. Using a flat phase pattern and large iris diameter, the

camera was positioned in the focus of the $f = 400$ mm achromat. The pinhole was then positioned at an equal distance from the achromat.

Using the top-hat phase pattern, the beam was aligned on the SLM to produce a symmetric PSF. Then the iris diameter and EOM phase were optimized to maximize the contrast of the 3D-donut in focus. The contrast was further maximized by aligning the angle of the half wave plate and the EOM phase.

The pinhole, mounted in an x-y translation stage (ST1XY-D/M, Thorlabs), was adjusted in the lateral directions to maximize the signal on the photo diode using a flat SLM phase pattern.

Phase drift measurements

To monitor the phase drift of the EOM (Supplementary Fig. 7), we split off 10% of the laser light after the EOM with a non-polarizing beam splitter, passed that beam through a Glan-Thompson polarizer (GTH10M-A, Thorlabs) oriented orthogonal to the first one before the EOM and monitored the intensity with an amplified photo diode (PDA100A2, Thorlabs). We repeatedly scanned the EOM voltage around the intensity minimum and fitted the minimum with a quadratic function to extract the zero-point voltage V_0 .

Acknowledgements

We thank Giuseppe Vicidomini and Eli Slenders for their kind feedback on the manuscript, Luciano Masullo for help with the CRB calculations and the EMBL electronic and mechanic workshops for contributing to the setup. This work was supported by H2020 Marie Skłodowska-Curie Actions (RobMin grant no. 101031734 to T.D.); the European Research Council (grant no. ERC CoG-724489 to J.R.); and the European Molecular Biology Laboratory (T.D. and J.R.).

Author details

¹European Molecular Biology Laboratory, Cell Biology and Biophysics, Heidelberg, Germany. ²Max Perutz Labs, Vienna Biocenter Campus (VBC), Vienna, Austria. ³University of Vienna, Center for Molecular Biology, Department of Structural and Computational Biology, Vienna, Austria. ⁴University of Vienna, Faculty of Physics, Vienna, Austria

Data availability

Simulated PSFs, scripts to calculate CRBs and a script to calculate the polarization state are available at: <https://github.com/ries-lab/MINFLUXexcitation>.

Conflict of interest

The EMBL has deposited the European patent application 23193790.5 on the 28 July 2023 to protect this work. T.D. and J.R. are co-inventors.

Supplementary information The online version contains supplementary material available at <https://doi.org/10.1038/s41377-024-01487-1>.

Received: 28 January 2024 Revised: 6 May 2024 Accepted: 16 May 2024
Published online: 07 June 2024

References

1. Balzarotti, F. et al. Nanometer resolution imaging and tracking of fluorescent molecules with minimal photon fluxes. *Science* **355**, 606–612 (2017).

- Gwosch, K. C. et al. MINFLUX nanoscopy delivers 3D multicolor nanometer resolution in cells. *Nat. Methods* **17**, 217–224 (2020).
- Pape, J. K. et al. Multicolor 3D MINFLUX nanoscopy of mitochondrial MICOS proteins. *Proc. Natl Acad. Sci. USA* **117**, 20607–20614 (2020).
- Ostersehl, L. M. et al. DNA-PAINT MINFLUX nanoscopy. *Nat. Methods* **19**, 1072–1075 (2022).
- Eilers, Y., Ta, H., Gwosch, K. C., Balzarotti, F. & Hell, S. W. MINFLUX monitors rapid molecular jumps with superior spatiotemporal resolution. *Proc. Natl Acad. Sci.* **115**, 6117–6122 (2018).
- Wirth, J. O. et al. MINFLUX dissects the unimpeded walking of kinesin-1. *Science* **379**, 1004–1010 (2023).
- Deguchi, T. et al. Direct observation of motor protein stepping in living cells using MINFLUX. *Science* **379**, 1010–1015 (2023).
- Schmidt, R. et al. MINFLUX nanometer-scale 3D imaging and microsecond-range tracking on a common fluorescence microscope. *Nat. Commun.* **12**, 1478 (2021).
- Masullo, L. A. & Stefani, F. D. Multiphoton single-molecule localization by sequential excitation with light minima. *Light Sci. Appl* **11**, 70 (2022).
- Masullo, L. A. et al. Pulsed Interleaved MINFLUX. *Nano Lett.* **21**, 840–846 (2021).
- Zhan, Z. et al. Simultaneous super-resolution estimation of single-molecule position and orientation with minimal photon fluxes. *Opt. Express* **30**, 22051 (2022).
- Huang, Z. et al. Spectral Identification of Specific Photophysics of Cy5 by Means of Ensemble and Single Molecule Measurements. *J. Phys. Chem. A* **110**, 45–50 (2006).
- Widengren, J. & Schwille, P. Characterization of Photoinduced Isomerization and Back-Isomerization of the Cyanine Dye Cy5 by Fluorescence Correlation Spectroscopy. *J. Phys. Chem. A* **104**, 6416–6428 (2000).
- Haupts, U., Maiti, S., Schwille, P. & Webb, W. W. Dynamics of fluorescence fluctuations in green fluorescent protein observed by fluorescence correlation spectroscopy. *Proc. Natl Acad. Sci. USA* **95**, 13573–13578 (1998).
- Leutenegger, M., Rao, R., Leitgeb, R. A. & Lasser, T. Fast focus field calculations. *Opt. Express* **14**, 11277–11291 (2006).
- Engelhardt, T. MINFLUX Nanoscopy with Interferometric Approach. PhD Thesis, University of Heidelberg. 2023. <https://doi.org/10.11588/heidok00031212>.
- Masullo, L. A., Lopez, L. F. & Stefani, F. D. A common framework for single-molecule localization using sequential structured illumination. *Biophysical Rep.* **2**, 100036 (2022).